

A REMARKABLE MULTILOBE MOLECULAR OUTFLOW: ρ OPHIUCHI EAST, ASSOCIATED WITH IRAS 16293–2422

A. MIZUNO, Y. FUKUI, T. IWATA, AND S. NOZAWA
 Department of Astrophysics, Nagoya University

AND

T. TAKANO

Toyokawa Observatory, National Astronomical Observatory
 Received 1988 September 6; accepted 1989 December 5

ABSTRACT

Rho Ophiuchi East is one of the molecular outflows discovered in the Nagoya CO survey of star formation regions (Fukui *et al.*) and was independently discovered by Wootten and Loren. IRAS 16293–2422 is the driving source of the outflow. We have made a detailed observational study of this outflow source in the $J = 1-0$ and $J = 2-1$ transitions of carbon monoxide and in the $(J, K) = (1, 1)$ and $(2, 2)$ transitions of ammonia with angular resolutions of $17''$ – $80''$.

The high-velocity CO emission has been resolved into four compact separate lobes, consisting of two pairs of bipolar lobes, in addition to an extended monopolar blueshifted lobe. We present four possible interpretations for the multiple distribution of the high-velocity molecular gas: (1) three driving engines, (2) two driving engines with strong time variation, (3) two driving engines, one of which is precessing, and (4) dynamical interaction of the high-velocity gas with the dense cloud core. We show that precession does not reproduce the detailed distribution of the high-velocity gas, and we discuss the importance of the dynamical interaction of the outflow with the ambient molecular gas in formation of the CO lobes.

The NH_3 cloud has a size of $\sim 2.5 \times 2.5$, being peaked at $1.7'$ east of IRAS 16293–2422. This NH_3 peak is located just toward the edge of one of the compact blue CO lobes, showing a blueshift of $\sim 0.5 \text{ km s}^{-1}$ from the rest of the NH_3 cloud. The momentum involved in the NH_3 peak is nearly equal to that of the CO lobe. Thus, we suggest that the CO lobe has dynamically interacted with the NH_3 core, resulting in the acceleration of the NH_3 core by 0.5 km s^{-1} . This provides the first direct evidence for an outflow accelerating interstellar molecular gas, strongly suggesting the dynamical importance of outflow in cloud cores where stars are formed.

Subject headings: interstellar: molecules — nebulae: individual (ρ Oph E)

I. INTRODUCTION

Rho Ophiuchi East is one of the bipolar outflows recently found with the Nagoya 4 m radio telescope in an unbiased ^{12}CO and ^{13}CO $J = 1-0$ survey of star formation regions (Fukui *et al.* 1986; Fukui 1989). This outflow is located $\sim 1.5'$ east of the ρ Ophiuchi main cloud at a distance of 160 pc (Whittet 1974), and is associated with an IRAS point source IRAS 16293–2422, whose infrared luminosity is $\sim 27 L_\odot$ (Mundy, Wilking, and Myers 1986). The outflow was independently discovered by Wootten and Loren (1987).

IRAS 16293–2422 is embedded in a very dense molecular cloud core mapped in the CS $J = 5-4$ emission (Walker *et al.* 1986) and has an unusually cold infrared spectrum, which can be fitted by a single ~ 40 K blackbody spectrum (Mundy, Wilking, and Myers 1986). A 2.7 mm continuum interferometry by Mundy *et al.* revealed a compact elongated dust cloud with a size of $\sim 1800 \times < 800$ AU toward IRAS 16293–2422. This dust cloud may be rapidly rotating, as suggested by spectroscopic interferometry of the ^{13}CO $J = 1-0$ emission (Mundy, Wilking, and Myers 1986). Asymmetric sharp self-absorption features in the CS $J = 5-4$ line profiles were interpreted in terms of infalling molecular material around IRAS 16293–2422 in the protostellar stage. Higher angular resolution CS $J = 3-2$ data, however, suggest that the CS cloud may be better interpreted in terms of rotation rather than infall (Menten *et al.* 1987). Although the kinematical property of the dense cloud is still controversial, the very cold

dust temperature strongly suggests that IRAS 16293–2422 is one of the best candidates of a solar-type protostar.

Until now, two groups have mapped the CO outflow (Fukui *et al.* 1986; Wootten and Loren 1987). Fukui *et al.* (1986) showed that the outflow is elongated in the east-west direction with a size of $\sim 13' \times 6'$ in the ^{12}CO $J = 1-0$ emission with a $2.7'$ beam of the Nagoya 4 m radio telescope, whereas Wootten and Loren (1987) observed the central $8' \times 5'$ area around the IRAS source on the ^{12}CO $J = 2-1$ emission with $1.3'$ resolution. At a distance of 160 pc, $1'$ corresponds to 0.05 pc. A further detailed observational study of this outflow has been highly desirable, because the resolution of these maps is still too coarse to investigate the role of the outflow activity in the star formation process compared with the previous observations of the dense core around IRAS 16293–2422.

In this paper we present detailed observations of the CO outflow and the associated ammonia cloud. In § II we describe the observations. Sections III and IV are devoted to the description of results for the CO outflow and the ammonia cloud, respectively. In § V we present possible interpretations of the outflow morphology and discuss the importance of the dynamical interaction of the outflow with the ambient gas cloud.

II. OBSERVATIONS

The ^{12}CO $J = 2-1$ spectra were obtained with the 4.9 m millimeter-wave telescope at Millimeter Wave Observatory,

Fort Davis, in 1987 March and April. Pointing accuracy was better than $0.2''$ as determined by observing Jupiter. The half-power beamwidth of the telescope was $1.3''$ with forward scattering and spillover efficiency η_{fss} (Kutner and Ulich 1981) of 0.9 at 1.3 mm. The back-end spectrometer was a 256 channel filterbank with 250 kHz resolution. A region of $16' \times 7'$ in right ascension and declination toward IRAS 16293–2422 was mapped with a $1''$ grid spacing.

High-resolution ^{12}CO , ^{13}CO , and C^{18}O $J = 1-0$ observations were performed with the 45 m telescope at Nobeyama Radio Observatory¹ in 1986 February, May, and December. The half-power beamwidth of the telescope was $17''$ with a main-beam efficiency of 0.4 at 2.6 mm. Pointing accuracy was better than $5''$ as determined by observing a SiO maser source VX Sgr at 43 GHz every 2 hours. An area of $5' \times 4'$ in right ascension and declination was mapped in the ^{12}CO $J = 1-0$ emission with grid spacings of $15''-30''$, and the ^{13}CO $J = 1-0$ emission was observed toward five positions where the ^{12}CO $J = 1-0$ line wings are intense. Spectra were taken with acoustic-optical spectrometers with 40 kHz frequency resolution and 40 MHz bandwidth. Atmospheric extinction was corrected for by the chopper wheel method, and the abso-

¹ This work was carried out under the common-use observation program at the Nobeyama Radio Observatory (NRO). NRO, a branch of the National Astronomical Observatory, is a cosmic radio observatory open for outside users.

lute intensity scale was established by referring to M17SW, whose peak T_{R}^* values of the ^{12}CO , ^{13}CO , and C^{18}O $J = 1-0$ emission were taken to be 43.1, 14.9, and 2.4 K, respectively (Ulich and Haas 1976; Kutner and Ulich 1981).

The NH_3 ($J, K = (1, 1)$ and $(2, 2)$) data were obtained with the 100 m telescope at Effelsberg in 1986 March. The half-power beamwidth was $\sim 40''$ at 1.3 cm. The maser amplifier provided a system temperature including the atmosphere of 70 K. The back end was a 1024 channel autocorrelator, which was divided into two halves to observe the $(J, K) = (1, 1)$ and $(2, 2)$ transitions simultaneously. The velocity resolution was 0.16 km s^{-1} , and the total velocity coverage for each line was 80 km s^{-1} . Intensity calibration was done by observing standard intensity calibrators, 3C 123 and 3C 161. More details of this facility are described, for instance, in Takano *et al.* (1986).

III. RESULTS ON THE CO OUTFLOW

a) ^{12}CO $J = 2-1$ Observations

Figure 1a shows the distribution of the high-velocity ^{12}CO $J = 2-1$ emission. The blue lobe with a size of $\sim 13' \times 4'$ in major and minor axes is highly collimated in the east-west direction. The blue lobe has three parts, i.e., two strong peaks at $\sim 3'$ southwest and $\sim 2'$ east, and a weaker peak at $\sim 6'$ east of IRAS 16293–2422. The red lobe is elongated in the northeast-southwest direction with a size of $\sim 5' \times 3'$ and is localized within $\sim 4'$ of IRAS 16293–2422, much more compact than the blue lobe. Figure 1b reproduces the ^{12}CO $J = 1-0$ distribution obtained with the Nagoya 4 m radio telescope (Fukui *et al.* 1986) for comparison. The CO lobes in the $J = 1-0$ map are more extended in width than those in the $J = 2-1$ map, probably because of the difference in the beam size. In addition, the $J = 2-1$ peaks of the CO lobes are not apparent in the $J = 1-0$ map, suggesting that their distributions are even more compact than the $J = 2-1$ beam size.

Figure 2 shows a diagram of right ascension versus velocity at the declination of IRAS 16293–2422. Near the IRAS source, at $\Delta(\text{R.A.}) = -2'$ to $4'$, the high-velocity wings are prominent, being characterized by a large velocity shift of $\gtrsim 10 \text{ km s}^{-1}$ from the typical peak velocity of the ambient cloud,

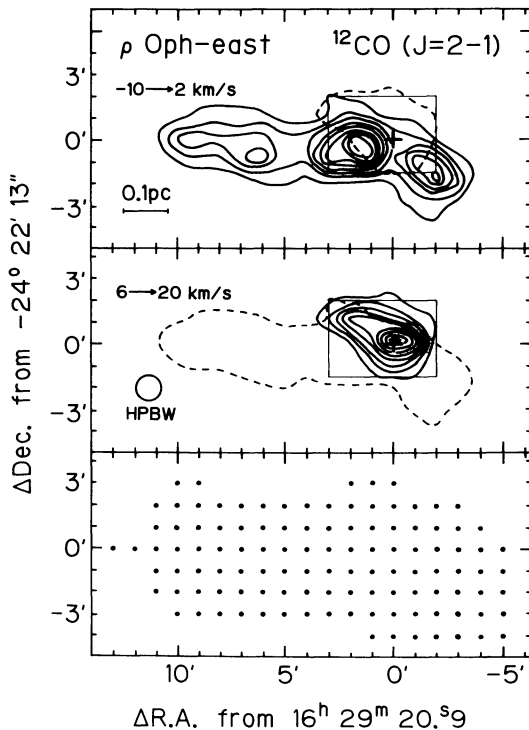


FIG. 1a

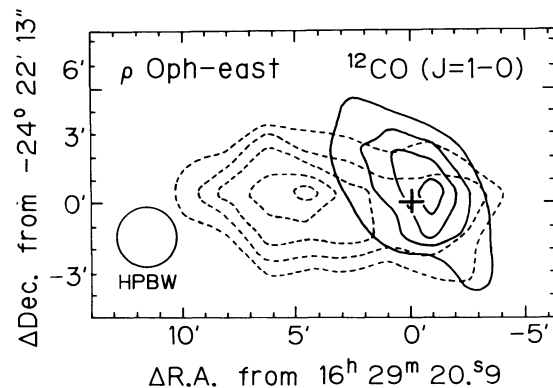


FIG. 1b

FIG. 1.—(a) Contour maps of ρ Oph East taken with the MWO 4.9 m telescope showing the distribution of the integrated intensity ($\int T_{\text{R}}^* dv$) of the ^{12}CO $J = 2-1$ transition. The velocity range for the blue wing is -10 to 2 km s^{-1} (top), and that for the red wing is 6 to 20 km s^{-1} (middle). Dots denote the observed positions (bottom). The offset center is the position of IRAS 16293–2422 [R.A.(1950) = $16^{\text{h}}29^{\text{m}}20.9^{\text{s}}$, decl.(1950) = $-24^{\circ}22'13''$] indicated by a cross. Contours extend from 4.0 K km s^{-1} with a 4.0 K km s^{-1} step. The lowest contours of the red wing (top) and the blue wing (middle) are superposed as dashed lines. Squares denote the observed region with the NRO 45 m telescope. (b) Contour map of the high-velocity wing in the ^{12}CO $J = 1-0$ transition of ρ Oph East taken with the Nagoya 4 m radio telescope. The velocity range of the blue wing (dashed contours) is -1 to 2 km s^{-1} , and that for the red wing (solid contours) is 6 to 9 km s^{-1} . Contours are every 1.0 K km s^{-1} . The offset center is the same as in (a)

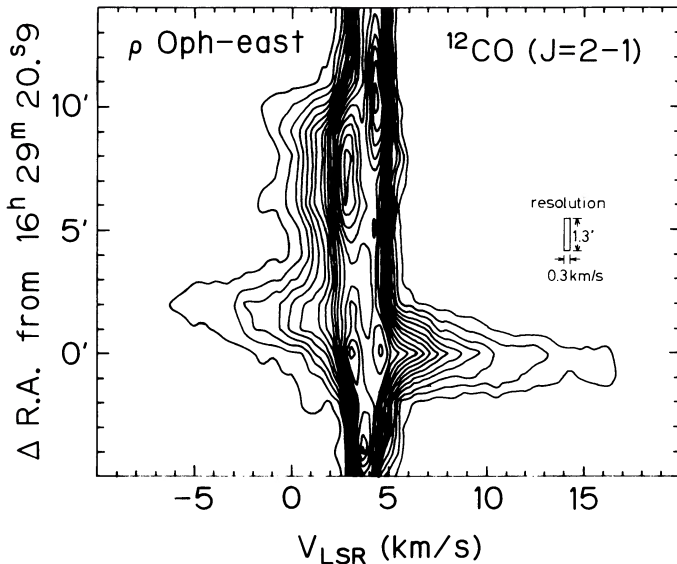


FIG. 2.—R.A. vs. velocity diagram of $^{12}\text{CO } J=2-1$ at decl. $-24^{\circ}22'13''$. The velocity resolution is 0.3 km s^{-1} . Contours extend from 1.1 K with a 1.1 K step.

$V_{\text{LSR}} \cong 4 \text{ km s}^{-1}$. On the other hand, weaker blueshifted wing emission is extended from $\Delta(\text{R.A.}) = 4'$ to $\Delta(\text{R.A.}) = 11'$ with a smaller velocity shift than that in the central region. The maximum velocity shift of this extended blue lobe is $\sim 6 \text{ km s}^{-1}$. On the west of the *IRAS* source there is no indication of such a weaker extended red lobe at an intensity level of 0.4 K with 0.3 km s^{-1} velocity resolution. In Figure 3 we show a $^{13}\text{CO } J=1-0$ map obtained with the Nagoya 4 m radio telescope. The ^{13}CO distribution is elongated in the east-west direction, having a sharp intensity gradient toward the west, and is part of a long filamentary cloud extending toward the east. The northwest boundary of the high-velocity CO emission well delineates that of the ^{13}CO cloud, suggesting that the

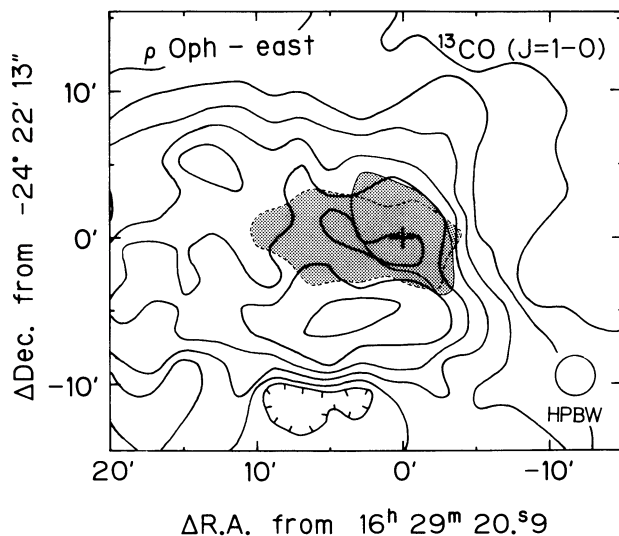


FIG. 3.— $^{13}\text{CO } J=1-0$ total intensity map taken with the Nagoya 4 m radio telescope. The ^{13}CO contours are every 5.0 K km s^{-1} from 5.0 K km s^{-1} . The stippled region denotes an area of $^{12}\text{CO } J=1-0$ high-velocity emission detected above 1.0 K km s^{-1} level with the Nagoya 4 m telescope.

extended red lobe may be missing because of the paucity of the ambient matter on the west.

b) ^{12}CO and $^{13}\text{CO } J=1-0$ Observations

Figure 4 shows a $^{12}\text{CO } J=1-0$ map obtained with the 45 m telescope toward the central region indicated as a square in Figure 1a. These high-resolution observations have resolved the red lobe in Figure 1a into two distinctly separate lobes, and have revealed the detailed distribution of the blue lobe. We shall call the two compact red lobes the “NE-red” and “W-red” lobes, and the two compact blue lobes, the “E-blue” and “SW-blue” lobes, respectively. Although the SW-blue lobe, the largest one among the four compact lobes, is not fully covered in Figure 4, Figure 1a shows that the SW-blue lobe is also compact with a radius of $\sim 4'$. These compact CO lobes in the $\sim 7' \times 5'$ region are shown schematically in Figure 5. Thus, we conclude that ρ Oph East consists of five outflow lobes, four of which are compact, and that all of them apparently emanate from *IRAS* 16293–2422.

We show typical line profiles in Figure 6. We calculated physical parameters of each CO lobe from the $J=1-0$ ^{12}CO and ^{13}CO data, except for the SW-blue lobe, by assuming local thermodynamic equilibrium (LTE) and $[\text{H}_2]/[^{13}\text{CO}] = 5 \times 10^5$ (Dickman 1978) (Table 1). For the SW-blue lobe, which was not observed in the ^{13}CO emission, we calculated physical parameters by assuming that ^{12}CO optical depth is equal to 4, the average optical depth of the W-red lobe, and that an abundance ratio of $[\text{H}_2]/[^{12}\text{CO}]$ is 1×10^4 . The mass, momentum, and mechanical luminosity in Table 1 are geometrical means of upper and lower limits calculated as follows. The upper limits were calculated by assuming that all the high-velocity gas in a lobe is moving with the same spatial velocity, V_{char} , the maximum velocity shift of the $^{12}\text{CO } J=1-0$ emission from $V_{\text{LSR}} = 4 \text{ km s}^{-1}$ at 1σ noise level, and that observed radial velocities vary only as a result of the projection effect.

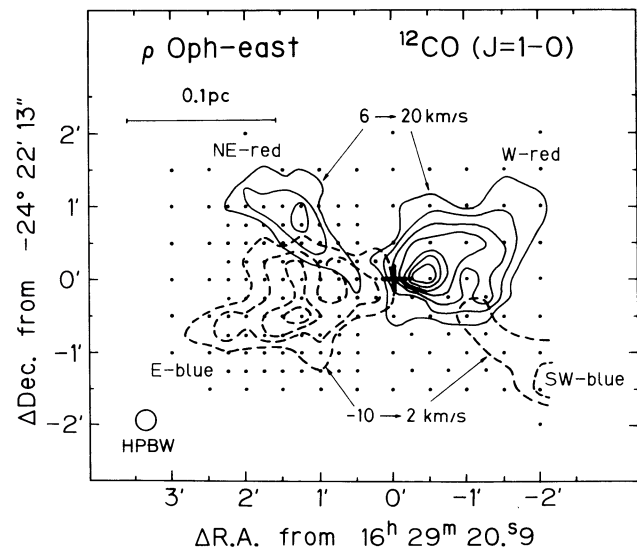


FIG. 4.—High-resolution integrated intensity map of the $^{12}\text{CO } J=1-0$ transition taken with the NRO 45 m telescope. The blue wings (dashed contours) and the red wings (solid contours) are integrated from -10 to 2 km s^{-1} and from 6 to 20 km s^{-1} , respectively. Contours extend from 10.8 K km s^{-1} with a 5.4 K km s^{-1} step. Dots denote the observed positions, and the cross marks the position of *IRAS* 16293–2422.

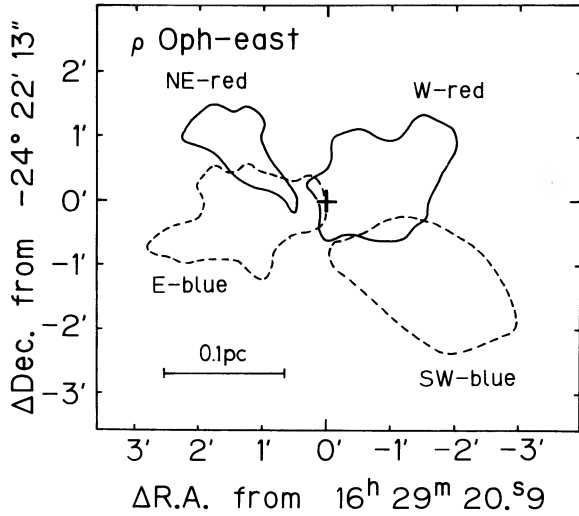


FIG. 5.—Schematic view of the four compact outflow lobes indicated as contours of $^{12}\text{CO } J=1-0$ emission at the 10.8 K km s^{-1} level except for the SW-blue lobe. The SW-blue lobe is indicated as a $^{12}\text{CO } J=2-1$ contour at 12.0 K km s^{-1} . The cross marks the position of IRAS 16293–2422.

On the other hand, for the lower limits, we assumed that the actual spatial velocity is equal to the observed radial velocity. We did not make any allowance for possible contribution from the low-velocity spectral line core as was done by other authors (e.g., Margulis and Lada 1985), because it is in general impossible to correct the physical parameters appropriately for the projection effect. Thus we consider that the listed values in Table 1 give lower limits. More details of these calculations are described in Iwata, Fukui, and Ogawa (1988).

The time scales and mechanical luminosities of the E-blue and W-red lobes are similar, and so are those of the SW-blue and NE-red lobes. Moreover, Figure 4 shows that the SW-blue and NE-red lobes are more highly collimated than the E-blue and W-red lobes; the collimation degrees of both the SW-blue and NE-red lobes are 2.6, whereas those of the E-blue and W-red lobes are 1.7. Taking these characteristics of the CO

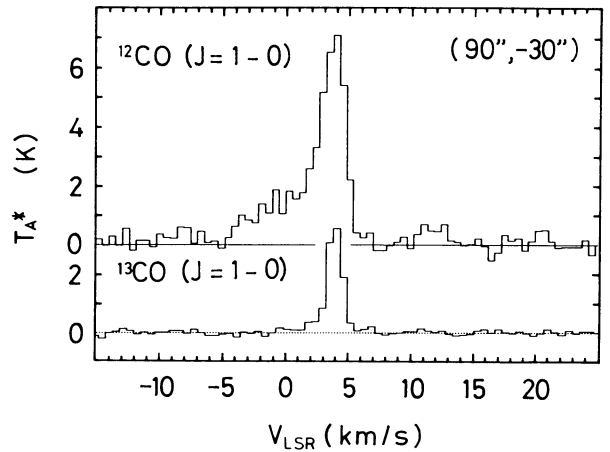
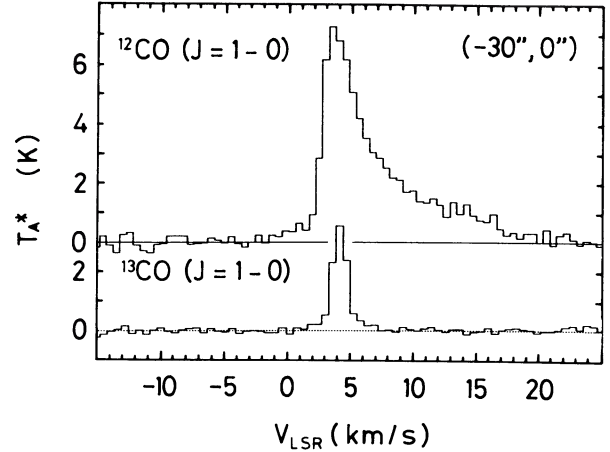


FIG. 6.— ^{12}CO and $^{13}\text{CO } J=1-0$ profiles at $(\Delta(\text{R.A.}), \Delta(\text{decl.})) = (90'', -30'')$ and $(-30'', 0'')$, where the blue and red wing intensities are prominent. The offset center is the IRAS position.

TABLE 1
PHYSICAL PARAMETERS OF FIVE OUTFLOW LOBES

Outflow Lobe	$V_{\text{char}}^{\text{a}}$ (km s^{-1})	Mass ^b (M_{\odot})	Momentum ^{b,c} ($M_{\odot} \text{ km s}^{-1}$)	Energy ^{b,c} (ergs)	Mechanical Luminosity ^{b,c} (L_{\odot})	Radius ^d (pc)	Dynamical Time Scale ^e (yr)
Compact outflow:							
E-blue	14	0.2	1.3	1×10^{44}	0.08	0.09	6×10^3
W-red	16	0.09	0.6	6×10^{43}	0.07	0.07	4×10^3
SW-blue	14	0.04 ^f	0.4 ^f	$4 \times 10^{43\text{f}}$	0.02 ^{f,g}	0.2 ^g	$1.4 \times 10^{4\text{h}}$
NE-red	12	0.06	0.5	3×10^{43}	0.01	0.11	9×10^3
Extended outflow:							
Blue	6	0.2	0.9	4×10^{43}	0.003	0.5	9×10^4

^a Maximum velocity shift of the $^{12}\text{CO } J=1-0$ emission from $V_{\text{LSR}} = 4 \text{ km s}^{-1}$ at 1σ noise level.

^b The excitation temperature is assumed to be 15 K.

^c Geometrical mean of upper and lower limits. The upper limits are computed by assuming that the high-velocity gas is moving with the same velocity, V_{char} . The lower limits are computed by assuming that the actual spatial velocity is equal to the observed radial velocity.

^d The radius is defined as the maximum separation from the IRAS source to a point where the wing intensity falls to half of the peak intensity.

^e The dynamical time scale is computed by dividing the radius by V_{char} .

^f These quantities are derived assuming that the optical depth of the $^{12}\text{CO } J=1-0$ emission is equal to 4, the average optical depth of the W-red lobe, and that $[\text{H}_2]/[^{12}\text{CO}] = 1 \times 10^4$.

^g The radius of this lobe is estimated from the $^{12}\text{CO } J=2-1$ map in Fig. 1a.

^h Derived from the spatial extent and velocity width of the $^{12}\text{CO } J=2-1$ data.

lobes into account, we consider that the E-blue and W-red lobes form a bipolar outflow and that the SW-blue and NE-red lobes form another bipolar outflow.

There is a known case that shows multiple CO lobe distributions other than ρ Oph East. It is L723 (Goldsmith *et al.* 1984). The L723 outflow has two pairs of bipolar outflows that may be produced by a mechanism similar to that for ρ Oph East. The ρ Oph East outflow has the most complicated lobe distribution among the known outflows, since it has an extended lobe in addition to two compact bipolar outflows.

IV. RESULTS ON THE DENSE CLOUD CORE

a) Ammonia Emission as a Probe of the Dense Gas around IRAS 16293–2422

In order to probe the distribution of the dense molecular gas around IRAS 16293–2422, we choose the ammonia (1, 1) and (2, 2) spectra that have much smaller optical depths than other spectra like HCO^+ $J=1-0$, CS $J=2-1$, and HCN $J=1-0$. Figure 7 shows molecular spectra of C^{18}O $J=1-0$, HCO^+

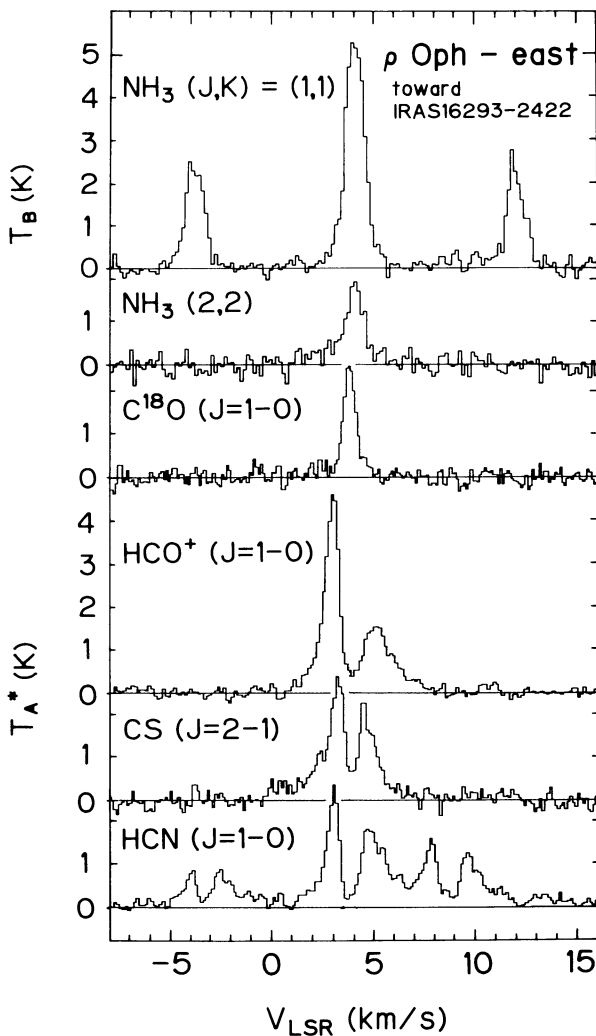


FIG. 7.—Line profiles of NH_3 (J, K) = (1, 1), (2, 2), C^{18}O $J=1-0$, HCO^+ $J=1-0$, CS $J=2-1$, and HCN $J=1-0$ transitions obtained toward IRAS 16293–2422. The intensity scale for NH_3 (J, K) = (1, 1) and (2, 2) is the main-beam brightness temperature, T_B , and that for C^{18}O , HCO^+ , CS, and HCN is the corrected antenna temperature, T_A^* (Kutner and Ulich 1981).

$J=1-0$, CS $J=2-1$, and HCN $J=1-0$ taken with the 45 m telescope, as well as the ammonia spectra, toward the IRAS position. Three of them, CS $J=2-1$, HCO^+ $J=1-0$, and HCN $J=1-0$, show very deep self-absorption features at $V_{\text{LSR}} \sim 3.5-4.0 \text{ km s}^{-1}$, indicating that these spectral lines are heavily masked by the foreground cool molecular gas. It may be noteworthy that even the satellite hyperfine components of HCN show deep self-absorption. Spatial distributions of these three spectra show that this cool molecular gas responsible for the self-absorption is extended over the dense gas cloud (Mizuno, Iwata, and Fukui 1990). On the other hand, the ammonia and C^{18}O spectra show no sign of self-absorption. Peak optical depth of the C^{18}O spectrum is estimated to be 0.5 by assuming an excitation temperature of 16 K estimated from the peak $J=1-0$ ^{12}CO intensity. It is, however, very unlikely that the C^{18}O emission reflects the inner dense part of the cloud core because that transition is easily excited in a tenuous envelope of a molecular cloud core, having densities less than 10^3 cm^{-3} . In fact, the spatial distribution of the C^{18}O emission is more extended than the NH_3 cloud shown in Figure 8 (see Table 3), and the peak velocity of ammonia is $\sim 0.2-0.3 \text{ km s}^{-1}$ higher than that of the C^{18}O spectra toward IRAS 16293–2422, supporting the conjecture that the two spectral lines originate in different volumes in space. On the contrary, the ammonia transitions are excited at densities greater than 10^4 cm^{-3} (e.g., Ho and Townes 1983), and the ammonia cloud is localized within $4'$ of IRAS 16293–2422 as shown in Figure 8. We therefore consider that the ammonia emission reflects the dense cloud core around IRAS 16293–2422.

b) Ammonia Observations

Figure 8 shows the distribution of the peak main-beam brightness temperature, T_B , of the NH_3 (J, K) = (1, 1) emission. IRAS 16293–2422 is located at the western edge of the NH_3 cloud, and the distribution is extended toward the east by ~ 2.5 from IRAS 16293–2422. The emission peak is located at ~ 1.7 ($\sim 0.08 \text{ pc}$) east of IRAS 16293–2422, whereas there is no

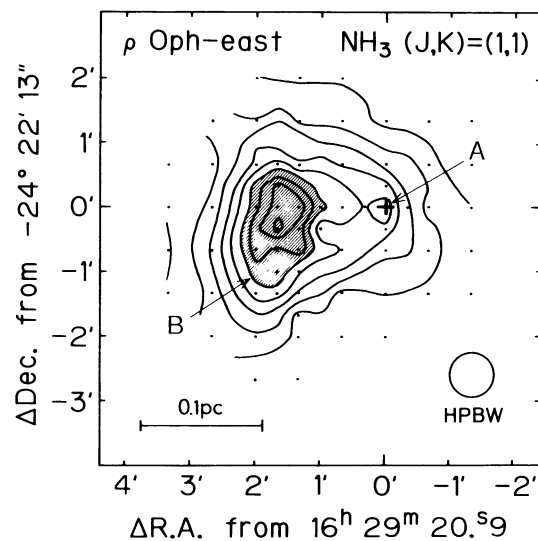


FIG. 8.—Map of the peak main-beam brightness temperature of NH_3 (J, K) = (1, 1) inversion transition taken with the Effelsberg 100 m telescope. Contours extend from 0.9 K with a 0.9 K step. The cross marks the position of IRAS 16293–2422, denoted A. The shaded region indicates the NH_3 core, denoted B.

TABLE 2
PHYSICAL PARAMETERS OF DENSE CORES

Parameter	NH ₃ Core	IRAS Source
Observed:		
Size	0.09 × 0.05 pc	...
$T_B(1, 1)$ (K)	8.4 ^a	5.2
$T_B(2, 2)$ (K)	3.6 ^a	1.7
$V_{\text{peak}}(1, 1)$ (km s ⁻¹) ^b	3.6	4.2
$V_{\text{peak}}(2, 2)$ (km s ⁻¹) ^b	3.6	4.1
$V_{\text{peak}}(\text{C}^{18}\text{O})$ (km s ⁻¹) ^c	3.6	3.9
$\Delta V(\text{NH}_3(1, 1))$ (km s ⁻¹)	0.4–0.5	0.7
$\Delta V(\text{C}^{18}\text{O})$ (km s ⁻¹)	0.8–0.9	0.8
Calculated:		
$\tau_T(1, 1)$ ^d	7.8	4.8
$\tau_{\text{main}}(1, 1)$ ^e	1.8	1.1
$\tau_{\text{main}}(2, 2)$ ^f	0.4	0.2
$\eta_f N(\text{NH}_3)$ (cm ⁻²) ^d	1.8×10^{15a}	8×10^{14}
T_{ROT} (K) ^d	12	15

^a Observed or derived value at the NH₃ peak [$\Delta(\text{R.A.}) = -100''$; $\Delta(\text{decl.}) = -20''$].

^b Radial velocity of the main hyperfine line peak derived by Gaussian fitting.

^c Radial velocity of the C¹⁸O $J = 1-0$ emission derived by Gaussian fitting.

^d $\tau_T(1, 1)$, $\eta_f N(\text{NH}_3)$, and T_{ROT} are calculated by using a nonlinear fitting program (Ungerechts, Walmsley, and Winnewisser 1980; Pauls *et al.* 1983).

^e Optical depth of the NH₃ (1, 1) main hyperfine line, $\tau_{\text{main}}(1, 1)$, is estimated by $\tau_{\text{main}}(1, 1) = 0.23\tau_T(1, 1)$ (Ungerechts, Walmsley, and Winnewisser 1980).

^f $\tau_{\text{main}}(2, 2)$ was calculated from the following equation on the assumption that $T_{\text{ex}}(1, 1)$ and $T_{\text{ex}}(2, 2)$ are equal:

$$T_B(2, 2)/T_B(1, 1) = \{1 - \exp[-\tau_{\text{main}}(2, 2)]\} / \{1 - \exp[-\tau_{\text{main}}(1, 1)]\}.$$

significant enhancement of the NH₃ intensity at the IRAS position. The region with the stronger NH₃ emission, where T_B is higher than 5.4 K, is elongated in the north-south direction, and we shall, hereafter, refer to this region as the “NH₃ core.”

We calculated the total optical depth, τ_T , and rotation temperature, T_{ROT} , of NH₃ by fitting LTE one Gaussian component to the NH₃ (1, 1) and (2, 2) spectra by using a nonlinear fitting program (Ungerechts, Walmsley, and Winnewisser 1980; Pauls *et al.* 1983). Physical parameters at the NH₃ core and IRAS 16293–2422 are listed in Table 2. The rotation temperature between the (1, 1) and (2, 2) levels is almost uniform, within 11–15 K, over the whole NH₃ emitting region. T_{ROT} at the IRAS source, ~ 15 K, is a little higher than at the NH₃ core, ~ 12 K. T_{ROT} for the narrow component shows a good agreement with that estimated by the previous authors

(Menten *et al.* 1987). In Figure 7 a broad pedestal feature can be seen on the blueshifted side for both (1, 1) and (2, 2) spectra. The signal-to-noise ratio of our data, however, is not good enough to estimate physical parameters of the broad feature, and we did not try to deconvolve the broad feature. Menten *et al.* (1987) claimed a high rotation temperature of 39(+50, -13) K for the broad component ($\Delta v_{1/2} \sim 2$ km s⁻¹) by using the spectra whose rms noise is very similar to ours, although their estimate for the broad component is also ambiguous as mentioned by the authors. For particle densities around 10^5 cm⁻³, kinetic temperature is nearly equal to the rotation temperature (e.g., Walmsley and Ungerechts 1983). Thus, T_{ROT} is considered to be equal to the kinetic temperature. The beam-averaged column densities are calculated from the above parameters under the assumption $T_{\text{ex}} \gg T_{\text{bg}}$. The beam-averaged column densities, $\eta_f N(\text{NH}_3)$, at the IRAS source and the NH₃ core are 8×10^{14} and 1.8×10^{15} cm⁻², respectively. Toward the NH₃ core, we infer that the beam filling factor, η_f , is nearly equal to unity, since the brightness temperature is close to the value expected from the rotation temperature.

We need the ammonia abundance in order to convert the ammonia column density into the total molecular hydrogen column density. About 30 dark cloud cores have been mapped by ammonia (e.g., Myers and Benson 1983; Ho and Townes 1983), and the ammonia abundance is relatively well calibrated. We shall here adopt the values derived from observations of a number of dark clouds in Taurus and Ophiuchus by Benson and Myers (1983). The relative ammonia abundance in these regions ranges from 3×10^{-8} to 1×10^{-7} . For the range we calculated the total molecular mass and the average number density for the NH₃ core to be from 1.4 to 4.8 M_{\odot} , and from 1×10^5 to 4×10^4 cm⁻³, respectively. In order to justify our assumption of the NH₃ abundance, we may compare the NH₃ column density with that of C¹⁸O, which is perhaps more stable and is better correlated with H₂ than NH₃. We assumed that C¹⁸O abundance, $[\text{C}^{18}\text{O}]/[\text{H}_2]$, is 2×10^{-7} (Frerking, Langer, and Wilson 1982). At the NH₃ core, the C¹⁸O column density is estimated to be 7×10^{15} cm⁻², and that of NH₃ is 1.8×10^{15} cm⁻², resulting in the $[\text{NH}_3]/[\text{H}_2]$ ratio $\sim 6 \times 10^{-8}$. This value is to be considered as a lower limit, since the C¹⁸O emission samples larger volume along the line of sight than the NH₃ emission, as indicated in Table 3. The value is consistent with the NH₃ abundance derived by Benson and Myers (1983).

We note that Wootten and Loren (1987) derived the density of $\sim 10^6$ cm⁻³ by the LVG analysis of the DCO⁺ $J = 4-3$, $J = 3-2$, and $J = 2-1$ spectra at the peak position. This density

TABLE 3
COMPARISON OF THE PHYSICAL PARAMETERS DERIVED FROM ¹³CO, C¹⁸O, AND NH₃ OBSERVATIONS

Molecular Line	Cloud Size ^a	Mean Radius ^b (pc)	Mass (M_{\odot})	Mean Density ^c (cm ⁻³)
¹³ CO $J = 1-0$	25' × 14'	0.5	340	1×10^4
C ¹⁸ O $J = 1-0$	8' × 5'	0.2	80	3×10^4
NH ₃ ($J, K = (1,1), (2,2)$)	2.5 × 2.5	0.06	4	6×10^4

^a Cloud size is described as the diameters of the major and minor axes. The diameter is defined as the length between the two points where the intensities drop to half the maximum.

^b The mean radius was calculated as the geometrical mean of the radius of the major and minor axes.

^c The mean density was calculated by assuming that the sphere with derived mean radius includes the derived mass.

TABLE 4
COMPARISON OF THE ENERGETICS BETWEEN THE CO OUTFLOW
AND THE NH₃ CORE

Component	Mass (M_{\odot})	Momentum ($M_{\odot} \text{ km s}^{-1}$)	Energy (ergs)
CO E-blue lobe	0.2	1.3	1×10^{44}
NH ₃ core	2.6 ^a	1.3 ^b	7×10^{42}

^a Estimated by taking an abundance ratio of ammonia, $[\text{NH}_3]/[\text{H}_2]$, of 5.5×10^{-8} .

^b Expected momentum to accelerate the NH₃ core from $V_{\text{LSR}} = 4.1$ to 3.6 km s^{-1} .

is significantly higher than that derived from the NH₃ data above. It is, however, not clear whether such a high-density region is distributed uniformly over the core. It is probably more likely that the distribution of such a high-density region is highly clumpy, occupying a smaller volume fraction of the core. Such a clumpiness in DCO⁺ is consistent with the lower average density derived by NH₃, if we take account of the NH₃ beam filling factor close to unity as mentioned above. We shall, therefore, adopt the ammonia result as the core mass, and use a geometrical average of the values for the upper and lower limits derived from NH₃, $2.6 M_{\odot}$, in the following discussion (Table 4).

c) Comparison with the Other Maps

We note that the peak optical depth of the main component of the (1, 1) transition is moderately saturated, as shown by the optical depths of the main line, 1.1–1.8, in Table 2. This, however, does not imply that the (1, 1) distribution does not represent well the density distribution toward IRAS 16293–2422, because the optically thin (2, 2) distribution has a distribution very similar to the (1, 1) distribution. A difference between the (1, 1) and (2, 2) distributions is that intensity ratios of the NH₃ core to the IRAS position (peak A in Fig. 8) are 2 and 3 for the (1, 1) and (2, 2) spectra, respectively, suggesting that the (1, 1) distribution may be a little, but not significantly, saturated by an optical depth effect.

Wooten and Loren (1987) mapped the core in the DCO⁺ $J = 3-2$ and NH₃ (1, 1) emission with $30''$ – 1.25 beams. The two distributions having the primary peaks at B in Figure 8 are generally consistent with the present NH₃ core distribution, although the DCO⁺ emission was not detected toward IRAS 16293–2422. The DCO⁺ emission originates in regions with very high densities greater than 10^5 cm^{-3} , and is perhaps optically thin. The consistency supports our decision to use the ammonia (1, 1) emission to probe the mass distribution in the dense core peaking at B in Figure 8.

On the other hand, in the close vicinity, $\lesssim 0.01 \text{ pc}$, of the IRAS source (peak A in Fig. 8) there could be significant abundance changes in molecular tracers. Mundy, Wilking, and Myers (1986) found a very compact dust disk with a size of $1800 \times < 800 \text{ AU}$ ($\sim 11'' \times < 5''$) at the IRAS position with an interferometer in 2.7 mm continuum emission, although NH₃ and DCO⁺ data do not show a significant intensity enhancement just toward IRAS 16293–2422. They estimated the mass of the dust disk to be 0.9 – $6.0 M_{\odot}$ by fitting the IRAS 25–100 μm and 2.7 mm continuum data. The upper and lower limits correspond to a dust spectrum with λ^{-1} and λ^{-2} emissivity laws, respectively. It implies that the density of the dust disk amounts to $\sim 10^{8 \pm 0.5} \text{ cm}^{-3}$. This density is very much higher

than those which ordinary molecular spectra trace. From our NH₃ data, the mass included in $40''$ beam toward the IRAS source is ~ 0.2 – $0.5 M_{\odot}$. Menten *et al.* (1987) mapped the vicinity of the IRAS source in CS and C³⁴S $J = 3-2$ spectra with a $17''$ beam. They derived the mass in two ways: one is from a LVG analysis and the other is from a kinematic analysis. With the LVG analysis they derived only ~ 1 – $1.5 M_{\odot}$ for an emission core with a size of $30'' \times 35''$. This value does not contradict our estimate, if we take the uncertainty of ammonia relative abundance, 3×10^{-8} to 1×10^{-7} (Benson and Myers 1983), into consideration. On the other hand, a kinematic model fitting by modified Keplerian-like rotation with a heavily concentrated mass distribution by Menten *et al.* (1987) provides a larger mass, ~ 5 – $6 M_{\odot}$. Even in CS observations by Menten *et al.* (1987), the highly concentrated dust disk is missed with the LVG analysis. Although NH₃ and CS single-dish observations are suitable for the dense cores with sizes of several tenths of a parsec and densities of 10^4 – 10^6 cm^{-3} , even more compact and higher density regions like the IRAS 16293–2422 dust disk of 10^8 cm^{-3} may be missed in these tracers. In this connection, it may be worthwhile to note that the present calibration of ammonia abundance in § IVb is made only for size scales $\gtrsim 0.1 \text{ pc}$ and may not be appropriate for circumstellar regions with size scales $\lesssim 0.01 \text{ pc}$.

In Table 3 we give a summary of the physical parameters of the ¹³CO, C¹⁸O, and NH₃ clouds derived from observations made with the 4 m and 100 m telescopes. We see that the NH₃ cloud is embedded in a lower density, more extended C¹⁸O cloud that is enveloped by the ¹³CO cloud shown in Figure 3. VLA observations revealed two bright spots of NH₃ in the NH₃ core, which may represent the densest condensations (Wooten and Loren 1987).

V. DISCUSSION

a) Driving Engines of the CO Outflow

As indicated in Figure 1a, the whole outflow region is completely sampled with a $1'$ grid spacing. We cannot, however, find a sign of the red extended lobe. In the following, we consider that the extended lobe is a monopolar outflow, and that it is driven by IRAS 16293–2422, for the following three reasons: (1) the extended blue lobe is well collimated, and its axis just points to the IRAS source, (2) the weak wing emission continues to the compact blue lobe in the ¹²CO $J = 2-1$ map (Fig. 1a), and (3) we do not find any other candidates of the driving engine within the sensitivity limits of the IRAS Point Source Catalog (IRAS Explanatory Supplement 1984) and POSS plates. A more sensitive survey is, however, certainly desired in order to investigate whether another driving source is embedded or not.

Rho Ophiuchi East is an enigmatic outflow, since it consists of five distinct CO lobes with different axes and dynamical time scales, apparently having a common driving source, IRAS 16293–2422. It is important to understand what is the origin of this remarkable distribution. An obvious possibility is that there are three driving engines for the east-west and northeast-southwest compact bipolar outflows and the extended monopolar outflow. It may be, however, somewhat unusual that three engines are located in a compact region of $\sim 1800 \times < 800 \text{ AU}$ radius, the extent of the dust cloud observed by the 2.7 mm interferometry, and there is no observational indication for triple stars in IRAS 16293–2422. We shall examine other possible explanations in the following.

A second possibility is that there are two driving engines, with stationary axes in the east-west and northeast-southwest directions. In this case, the extended monopolar outflow and the east-west compact bipolar outflow are both supposed to be driven by a common east-west-oriented engine, although the position angle of the extended lobe is somewhat different (by $\sim 10^\circ$) from that of the axis of the east-west compact outflow. An order-of-magnitude difference of time scales and mechanical luminosities between the extended monopolar outflow and the compact outflow (Table 1) implies that the outflow activity driven by the east-west-oriented engine may have been enhanced drastically in the last $\sim 10^4$ yr. Such drastic time variation has not been recognized in other outflows.

A third possibility is suggested by the symmetry property of the compact CO lobes. The locations of the two compact bipolar lobes (Fig. 5) in general show point symmetry with respect to IRAS 16293–2422. In addition, we note that the intensity distribution of the east-west compact lobes also shows point symmetry; at a position angle of 90° the extents of the E-blue and W-red lobes from IRAS 16293–2422 are ~ 1.5 , whereas with the increase of the position angle their extents increase up to ~ 2.5 at a position angle of 110° . Such point symmetry may be well explained by a precessing jet model such as that discussed by Fukue and Yokoo (1986). If we assume that the outflow velocity has been constant during the precession, the separations of the outflow lobes from the driving center are proportional to the time scales as observed. The direction of the precession is then counterclockwise, if we see the outflow axis from the east side of IRAS 16293–2422. The extended blue lobe probably requires another driving engine because its straight distribution does not match the precession.

A recent VLA 6 cm map toward IRAS 16293–2422 indicates that there are two radio continuum peaks within the 2.7 mm dust cloud (Wootten 1989). The stronger 6 cm peak is located ~ 750 AU (1×10^{16} cm) southeast of the 2.7 mm continuum peak, and the second 6 cm peak nearly coincides with the 2.7 mm peak. This observational result suggests that IRAS 16293–2422 may be a binary system. If one of the stars in this binary has a disk tilted to the orbital plane, the disk should undergo a precession due to the gravitational quadrupole interaction with the companion. If the molecular outflow is driven by a circumstellar disk as predicted in magnetohydrodynamical models (e.g., Uchida and Shibata 1985), the outflow can undergo precession.

In the following we shall describe a scenario for formation of the compact CO lobes by a precessing engine. We assume for simplicity that all the high-velocity gas is moving at a uniform velocity V_0 along the outflow axis and that outflow is highly collimated along the axis, having an opening angle much smaller than 10° . The observed radial velocity V_{char} is then given by $V_{\text{char}} = V_0 \cos \theta$, where θ is the inclination angle of the outflow axis to the line of sight. Taking into account the projection effect, we estimate the time scale of the northeast-southwest bipolar outflow to be $\sim 2 \times 10^4$ yr and that of the east-west outflow to be $\sim 9 \times 10^3$ yr. The difference between these two time scales becomes $\sim 1.1 \times 10^4$ yr. Within this time scale the outflow axis must have undergone precession by $\sim 130^\circ$, suggesting a precession period of $\sim 3 \times 10^4$ yr.

The period of precession caused by a gravitational quadrupole interaction P is theoretically given by the following equation (Pettersen 1977; Fukue and Yokoo 1986):

$$P = -1.3 M_d^{1/2} M_c^{-1} a^3 r^{-3/2} \cos^{-1} \beta \text{ yr}, \quad (1)$$

where M_d is the mass of the circumstellar disk, M_c is the mass of the companion, a is the separation between the circumstellar disk and the companion, r is the radius of the circumstellar disk, and β is an angle between the equatorial plane of the circumstellar disk and the binary orbital plane. M_d and M_c are in solar mass units, and a and r are in astronomical units. The minus sign indicates that the precession is inverse to that of the binary orbital rotation. The dust cloud is suggested to be rotating clockwise seen from the east side (Mundy, Wilking, and Myers 1986; Menten *et al.* 1987). The precession direction is, then predicted to be counterclockwise according to equation (1). The point-symmetric CO lobe distribution is in fact consistent with this precession direction. By adopting values consistent with the 2.7 mm interferometric data and other data, $M_d = 0.4 M_\odot$, $M_c = 2 M_\odot$, $a = 750$ AU, $r = 600$ AU, and $\beta = 60^\circ$, we provisionally estimated the precession period to be $\sim 4 \times 10^4$ yr. This period is nearly equal to that estimated from the present lobe morphology, $\sim 3 \times 10^4$ yr.

There are, however, some serious problems with the precession model. First, the northeast-southwest and east-west bipolar outflows are clearly separated, or there is no transient outflow component that connects the northeast-southwest and east-west outflows. This suggests that the outflow activity had a quiet phase between the northeast-southwest and east-west events, and that the intensity of the outflow activity must have changed drastically on a time scale of several thousands of years. This activity is not recognized. Second, if the east-west bipolar outflow was ejected after the northeast-southwest one had been ejected, the separation between the IRAS source and the NE-red lobe should have been larger than the maximum extent of the E-blue lobe. The NE-red lobe is, however, actually located close to the IRAS source, within 0.07 pc of IRAS 16293–2422, and the E-blue lobe has an extent comparable to the NE-red lobe. This is the most significant deviation of the compact CO lobes from point symmetry (see Fig. 5). Third, there is a question on the precession model itself, whether a disk may be dynamically stable over a time scale comparable to the precession period. Elaboration of the third point is beyond the scope of the present paper.

To summarize this subsection, we shall note that none of the above three possibilities can satisfactorily explain the CO lobe morphology. We shall discuss a fourth possibility in connection with the dynamical interaction of the outflow with the dense cloud in the next subsection.

b) Dynamical Interaction between the CO Outflow and the NH₃ Core

Molecular outflow is such an energetic phenomenon that outflow may have a significant dynamical influence on the ambient material. Dynamical interaction of outflow with ambient material has been noted in some cases (e.g., L1641 North, Fukui *et al.* 1988; NGC 2071 North, Iwata, Fukui, and Ogawa 1988; NGC 2071, Takano *et al.* 1986). The present case provides an even clearer example for such interactions.

We show superposition of the NH₃ core on the E-blue lobe and the NE-red lobe in Figures 9a and 9b, respectively. In Figure 9a the NH₃ core is located just toward the eastern edge of the E-blue lobe, strongly suggesting that the outflow is actually impacting the NH₃ core at that position. We see that the NH₃ peak shows an anticorrelation with the peak of the CO lobe. Figure 10, a right ascension versus velocity diagram at $\Delta(\text{decl.}) = -40''$, indicates that the NH₃ core has a discontinuous velocity shift of $\sim -0.5 \text{ km s}^{-1}$ from the rest of the

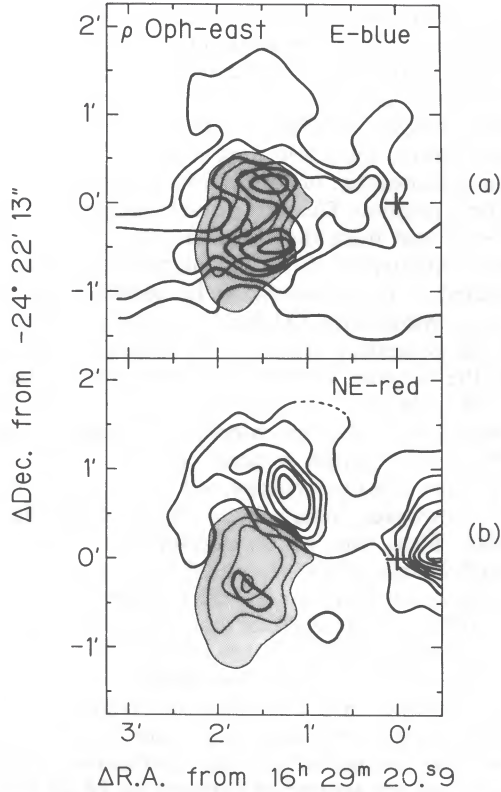


FIG. 9.—(a) NH_3 core (stippled region) superposed on the integrated intensity map of the E-blue lobe with a velocity interval from -4 to -1 km s^{-1} . $^{12}\text{CO } J = 1-0$ contours (thick solid lines) of the E-blue lobe extend from 1.4 K km s^{-1} with a 1.4 K km s^{-1} step, and the $\text{NH}_3(1, 1)$ contours (thin solid lines) extend from 5.4 K with a 0.9 K step. The cross marks the *IRAS* position. (b) NH_3 core superposed on the NE-red lobe with a velocity interval from 9 to 12 km s^{-1} . The contour levels of $^{12}\text{CO } J = 1-0$ and $\text{NH}_3(1, 1)$ are the same as in (a).

NH_3 cloud. We interpret that the velocity shift has been caused by the dynamical interaction of the outflow with the NH_3 core.

In order to test this interpretation more quantitatively, first we calculate momenta of the E-blue lobe and the NH_3 core projected on the line of sight, as listed in Table 4. The outflow momentum, $1.3 M_\odot \text{ km s}^{-1}$, is equal to that of the NH_3 core, $1.3 M_\odot \text{ km s}^{-1}$, indicating that the outflow has momentum large enough to cause the velocity shift if a significant portion of the outflow momentum is transferred to the NH_3 core. We note that the momentum of the CO outflow would become larger than the above value, because the outflow momentum does not take into account the possible contribution of the low-velocity spectral line core. Thus, the CO lobe momentum in Table 4 should be regarded as a lower limit.

Next we examine the effect of the outflow mechanical pressure. The outflow mechanical pressure is calculated as

$$P_{\text{fl}} = \rho_{\text{fl}} v_{\text{fl}}^2 = \frac{M v_{\text{fl}}^2}{4/3\pi R_{\text{fl}}^3} \sim 5 \times 10^{-8} \text{ dyn cm}^{-2} \quad (2)$$

from our data. The NH_3 core is expected to be in virial equilibrium if the outflow pressure, P_{fl} , satisfies

$$4\pi R^3 P \leq \frac{M(\Delta v)^2}{8 \ln 2} - \frac{3GM^2}{5R}, \quad (3)$$

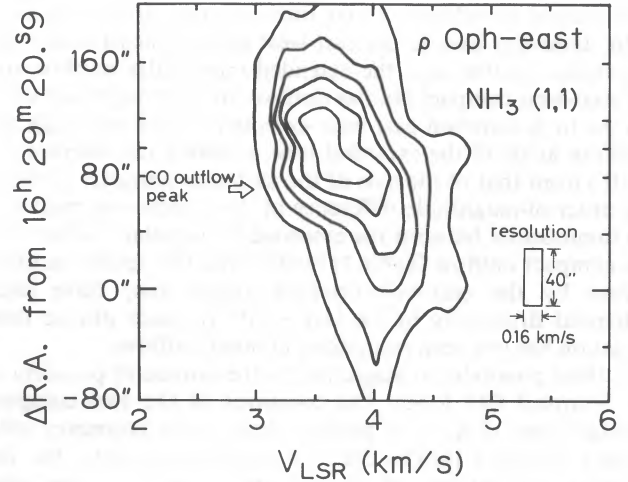


FIG. 10.—R.A. vs. velocity diagram of $\text{NH}_3(J, K) = (1, 1)$ along the east-west strip at $\Delta(\text{decl.}) = -40''$. The contours extend from 1.0 K with a 1.0 K step.

where Δv is the velocity width (FWHM) and R is the radius of the NH_3 core. However, the pressure term is two orders of magnitude larger than other terms; that is, the pressure term in virial equation (3) is calculated to be several times 10^{44} ergs, and both the kinetic energy and the gravitational energy are calculated to be several times 10^{42} ergs, from our data. Thus, the NH_3 core is not in equilibrium under the outflow mechanical pressure and is expected to be deformed or to collapse in the future.

The outflow pressure is so large that it should have affected the ambient gas distribution in the outflow dynamical time scale, $\sim 1 \times 10^4 \text{ yr}$. It is likely that the outflow formed a shocked layer and that the layer swept up the ambient gas. We roughly examine this effect of the outflow by a simplified one-dimensional model. We assume that the outflow pressure has been constant during $\sim 1 \times 10^4 \text{ yr}$, and is given by equation (2). The equation of motion is

$$\frac{d}{dt} [(M_{\text{sw}} + M_{\text{fl}})v_{\text{la}}] = \rho_{\text{fl}} v_{\text{fl}}^2 S, \quad (4)$$

where v_{la} is the velocity of the shocked layer, M_{sw} is the mass swept up by the layer, and M_{fl} is the amount of the outflowing gas which flows into the layer. We assume that M_{sw} and M_{fl} increase according to the following relations:

$$\frac{dM_{\text{sw}}}{dt} = \rho_0 v_{\text{la}} S, \quad (5)$$

$$\frac{dM_{\text{fl}}}{dt} = \rho_{\text{fl}} v_{\text{fl}} S, \quad (6)$$

where ρ_0 is the initial density of ambient gas and S is an area impacted by the outflow. From equations (4)–(6) we find that the shocked layer moves with a constant velocity:

$$v_{\text{la}} = \frac{2v_{\text{fl}}}{1 + (1 + 4\rho_0/\rho_{\text{fl}})^{1/2}}, \quad (7)$$

and swept-up mass for duration t is

$$M_{\text{sw}} = \frac{2v_{\text{fl}} \rho_0 S}{1 + (1 + 4\rho_0/\rho_{\text{fl}})^{1/2}} t. \quad (8)$$

TABLE 5
PHYSICAL PARAMETERS OF THE SWEEPED-UP LAYER^a

n_0^b (cm^{-3})	ρ_0^c (g cm^{-3})	V_{in}^d (km s^{-1})	L_{in}^d (pc)	M_{sw}^e (M_{\odot})
6×10^4	2×10^{-19}	4	0.04	0.8

^a The outflow mechanical pressure is assumed to be $5 \times 10^{-8} \text{ dyn cm}^{-2}$ from our CO data.

^b Mean number density of ambient gas before the shocked layer.

^c Mean density of ambient gas before the shocked layer.

^d Distance from the IRAS source to the shocked layer by 1×10^4 yr after the onset of the outflow.

^e Swept-up mass during 1×10^4 yr by the shocked layer.

In Table 5 we summarize the parameters of the layer. If we adopt the mean density, ρ_0 , as $6 \times 10^4 \text{ cm}^{-3}$ derived from our NH_3 data (see Table 3), the shocked layer may move by ~ 0.04 pc and sweep up $\sim 0.8 M_{\odot}$. We note that ~ 0.04 pc is a value comparable to the separation between the IRAS source and the western edge of the NH_3 core, and that $\sim 0.8 M_{\odot}$ is about one-third the mass of the NH_3 core. It is likely that some part of the NH_3 core mass may have been swept up by the outflow, and the elongated structure in the north-south direction may be formed as a result of such a sweeping-up process.

Figure 9b, on the other hand, indicates that the NE-red lobe shows a remarkable anticorrelation with the NH_3 core. This figure shows the CO integrated intensity down to a level as low as 1.4 K km s^{-1} , lower than that in Figure 4. At this low level, the CO lobe is curled toward the south just along the periphery of the NH_3 core, indicating a detailed anticorrelation. We therefore suggest that the CO lobe morphology may be determined by the existence of the ambient dense gas; i.e., the outflow gas may be excluded from a volume with higher density than its surroundings, the NH_3 core. A possibility that such an interaction determines the outflow morphology for ρ Oph East was also mentioned by Wootten and Loren (1987). Table 3, in fact, shows that the NH_3 cloud has a density larger than the ambient gas by factors of 2–6. Another remarkable example may be L1641 North, where the CO lobe has two peaks avoiding a dense gas ridge (Fukui *et al.* 1988).

In Figure 11 we present schematically a possible distribution

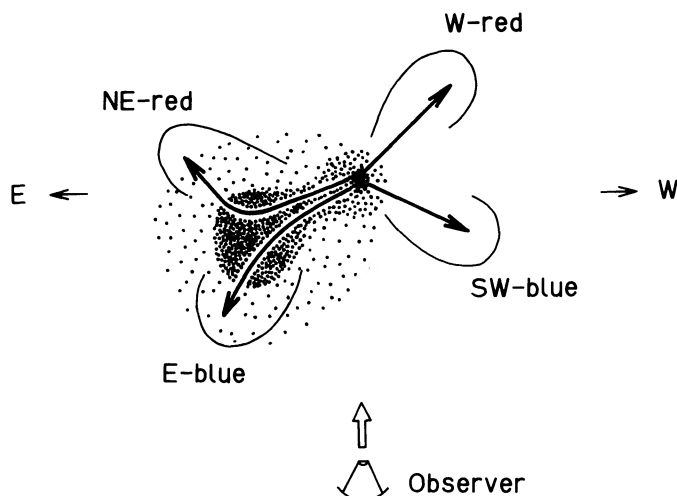


FIG. 11.—Schematic view of the dynamical interaction of the E-blue and NE-red lobes and the NH_3 core.

of the NE-red and E-blue lobes seen from the north. We suggest that a single blueshifted CO lobe is split into the NE-red and E-blue lobes as a result of the interaction with the NH_3 core, and that some of the original blueshifted gas avoids the collision with the NH_3 core, resulting in the formation of the extended monopolar blue lobe. Although the NH_3 cloud is not extended to the west of IRAS 16293–2422, there remains a possibility that dense molecular gas with densities much larger than 10^5 cm^{-3} may exist there, playing a role in forming the west and southwest lobes. In fact, the CS $J = 5-4$ observations indicate that there is a CS core with densities larger than 10^6 cm^{-3} toward IRAS 16293–2422, while its distribution is not well resolved with a $30''$ beam. In order to pursue the role of this dense cloud, which is not probed by the present $40''$ beam, higher resolution ($\lesssim 10''$) studies of this regions should be highly valuable in high-excitation spectra like the $J = 5-4$ CS line.

VI. CONCLUSION

We summarize the main conclusions of the present study as follows.

1. Rho Ophiuchi East consists of five separate CO lobes. Four of them are compact, localized within 0.2 pc of IRAS 16293–2422, and appear to form two pairs of bipolar outflows. Another is an extended blueshifted lobe with velocity shift smaller than those of the compact lobes. The dynamical time scales of the compact lobes are an order of magnitude smaller than that of the extended lobe, and their mechanical luminosities are 10 times larger than that of the extended lobe.

2. Rho Ophiuchi East is embedded in an extended ^{13}CO cloud elongated in the east-west direction, and is associated with a compact NH_3 cloud. The NH_3 cloud mass is estimated to be $\sim 4 M_{\odot}$ and is peaked at ~ 0.08 pc east of IRAS 16293–2422.

3. We examined three models in order to interpret the remarkably complicated distribution of the CO lobes. They are models of (1) three driving sources, (2) two driving sources with strong time variation, and (3) a precessing driving source. None of them, however, appears to explain the observations well.

4. There is a clear indication of dynamical interaction of the outflow with the NH_3 cloud core. The NH_3 core shows a velocity shift that is explained well as caused by the dynamical interaction with the outflow. Calculated momentum of the CO outflow is large enough to accelerate the NH_3 core. The outflow mechanical pressure is so large that the NH_3 core is not in equilibrium. It is likely that the north-south-elongated structure of the NH_3 core may be formed by the outflow.

5. As a fourth possibility for the multiple lobe distribution, we suggest dynamical interaction with the dense ambient cloud core having density larger than 10^6 cm^{-3} . In order to test this model we need observations of high-excitation emission with angular resolution higher than $10''$.

We wish to thank Neal J. Evans II for kindly allocating our telescope time at MWO and Elizabeth A. Lada for her assistance during our run. Thanks are also due to Gisbert Winnewisser for his hospitality extended to Y. F. and T. T. in West Germany, and to M. Miller for this help in observations at Effelsberg. We are grateful to T. Hanawa for useful discussion. This research was in part financially supported by grants-in-aid by the Ministry of Education, Science, and Culture of Japan (Nos. 58840004, 59420002, 60302014, 60790097, and 62420002).

REFERENCES

- Benson, P. J., and Myers, P. C. 1983, *Ap. J.*, **270**, 589.
 Dickman, R. L. 1978, *Ap. J. Suppl.*, **37**, 407.
 Frerking, M. A., Langer, W. D., and Wilson, R. W. 1982, *Ap. J.*, **262**, 590.
 Fukue, J., and Yokoo, T. 1986, *Nature*, **321**, 841.
 Fukui, Y. 1989, in *Low Mass Star Formation and Pre-Main Sequence Objects*, ed. B. Reipurth (Garching: ESO), p. 95.
 Fukui, Y., Sugitani, K., Takaba, H., Iwata, T., Mizuno, A., Ogawa, H., and Kawabata, K. 1986, *Ap. J. (Letters)*, **311**, L85.
 Fukui, Y., Takaba, H., Iwata, Y., and Mizuno, A. 1988, *Ap. J. (Letters)*, **325**, L13.
 Goldsmith, P. F., Snell, R. L., Hemeon-Heyer, M., and Langer, W. D. 1984, *Ap. J.*, **286**, 599.
 Ho, P. T. P., and Townes, C. H. 1983, *Ann. Rev. Astr. Ap.*, **21**, 239.
IRAS Catalogs and Atlases: Explanatory Supplement. 1984, ed. C. A. Beichman, G. Neugebauer, H. J. Habing, P. E. Clegg, and T. J. Chester (Washington, DC: GPO).
 Iwata, T., Fukui, Y., and Ogawa, H. 1988, *Ap. J.*, **325**, 372.
 Kutner, M. L., and Ulich, B. L. 1981, *Ap. J.*, **250**, 341.
 Margulis, M., and Lada, C. J. 1985, *Ap. J.*, **299**, 925.
 Menten, K. M., Serabyn, E., Güsten, R., and Wilson, T. L. 1987, *Astr. Ap.*, **177**, L57.
 Mizuno, A., Iwata, T., and Fukui, Y. 1990, in preparation.
 Mundy, L. G., Wilking, B. A., and Myers, S. T. 1986, *Ap. J. (Letters)*, **311**, L75.
 Myers, P. C., and Benson, P. J. 1983, *Ap. J.*, **266**, 309.
 Pauls, T. A., Wilson, J. L., Bieging, J. H., and Martin, R. N. 1983, *Astr. Ap.*, **124**, 23.
 Petterson, J. A. 1977, *Ap. J.*, **216**, 827.
 Takano, T., Stutzki, J., Fukui, Y., and Winnewisser, G. 1986, *Astr. Ap.*, **167**, 333.
 Uchida, Y., and Shibata, K. 1985, *Pub. Astr. Soc. Japan*, **37**, 515.
 Ulich, B. L., and Haas, R. W. 1976, *Ap. J. Suppl.*, **30**, 247.
 Ungerechts, H., Walmsley, C. M., and Winnewisser, G. 1980, *Astr. Ap.*, **88**, 259.
 Walker, C. K., Lada, C. J., Young, E. T., and Margulis, M. 1988, *Ap. J.*, **332**, 335.
 Walker, C. K., Lada, C. J., Young, E. T., Moaney, P. R., and Wilking, B. A. 1986, *Ap. J. (Letters)*, **309**, L47.
 Walmsley, C. M., and Ungerechts, H. 1983, *Astr. Ap.*, **122**, 164.
 Whittet, D. C. B. 1974, *M.N.R.A.S.*, **168**, 371.
 Wootten, A. 1989, *Ap. J.*, **337**, 858.
 Wootten, A., and Loren, R. B. 1987, *Ap. J.*, **317**, 220.

Note added in proof.—Walker *et al.* (1988) mapped in the $^{12}\text{CO } J = 2-1$ transition over a $280'' \times 200''$ region with $27''$ resolution. They also revealed the presence of four compact high-velocity lobes. They also claimed that there are two pairs of outflows driven by IRAS 16293 – 2422.

Y. FUKUI, T. IWATA, and A. MIZUNO: Department of Astrophysics, Nagoya University, Chikusa-ku, Nagoya, 464-01, Japan

S. NOZAWA: The Research Institute of Atmospherics, Nagoya University, Honohara, Toyokawa, 442, Japan

T. TAKANO: Toyokawa Observatory, National Astronomical Observatory, Toyokawa, 422, Japan